Journal of Energy Chemistry 65 (2022) 439–447

Contents lists available at ScienceDirect

Journal of Energy Chemistry

journal homepage: www.elsevier.com/locate/jechem

http://www.journals.elsevier.com/journal-of-energy-chemistry/

Synergistic effect of lithiophilic Zn nanoparticles and N-doping for stable Li metal anodes

Lei You [a,b], Shunlong Ju [a], Jianwen Liu [b], Guanglin Xia [a,*], Zaiping Guo [c,*], Xuebin Yu [a,*]

[a] Department of Materials Science, Fudan University, Shanghai 200433, China
[b] Hubei Collaborative Innovation Center for Advanced Organic Chemical Materials, Ministry-of-Education Key Laboratory for Synthesis and Applications of Organic Functional Molecules, College of Chemistry and Chemical Engineering, Hubei University, Wuhan 430062, Hubei, China
[c] School of Chemical Engineering & Advanced Materials, The University of Adelaide, Adelaide, SA 5005, Australia

ARTICLE INFO

Article history:
Received 27 December 2020
Revised 2 June 2021
Accepted 3 June 2021
Available online 8 June 2021

Keywords:
Li metal anodes
Zn nanoparticles
N-doping
Synergistic effect

ABSTRACT

Li metal is the most ideal anode material for next-generation high energy lithium-ion batteries. The uncontrollable growth of Li dendrites, however, hinders its practical application. Herein, we propose the adoption of Zn nanoparticles uniformly embedded in N-doped carbon polyhedra homogeneously built on carbon cloth (Zn@NC@CC) to prevent the formation of Li dendrites. Based on theoretical calculation and experimental observation, lithiophilic Zn nanoparticles and N-doping inside of the as-synthesized Zn@NC play a synergistic role in enhancing the adsorption capacity with Li, thus resulting in uniform Li deposition and complete suppression of Li dendrites. Moreover, the porous N-doped carbon polyhedras uniformly distributed on carbon cloth effectively relieves the volume change of Li upon repeated Li stripping/plating process, which contributes to preserving the structural integrity of the whole electrode and hence enhancing its long-term cycling stability. Benefiting from these synergistic effects, the Li-Zn@NC@CC electrode delivers a prolonged lifespan of over 1200 h at 1 mA cm^{-2} with an areal capacity of 1 mA h cm^{-2} in symmetric cells and high Coulombic efficiencies of 95.4% under an ultra-high capacity of 12 mA h cm^{-2}. Remarkably, Li-Zn@NC@CC//$LiFePO_4$ full cells deliver a high reversible capacity of 110.2 mA h g^{-1} at 1C over 200 cycles.

1. Introduction

With the rapid development of electronic devices, the traditional graphite anode of lithium-ion batteries can hardly meet the high-energy–density demand due to its limitation in specific capacity, so it is urgent to research and develop novel anodes with high capacity to replace them [1]. Li metal has been widely regarded as the most promising candidate for anode materials due to its high theoretical capacity of 3860 mA h g^{-1} and the ultra-low electrochemical anode potential (−3.04 V versus the standard hydrogen electrode) [2–4]. Despite these appealing advantages, the practical application of Li metal anode is severely hindered by the inevitable growth of dendritic and dead Li metal due to the uneven Li nucleation and the formation of unstable solid electrolyte interphase (SEI) layers. It leads to not only a low Coulombic efficiency and the quick decay of the capacity, but also, more importantly, serious safety hazards [5,6].

Accordingly, stabilizing the solid electrolyte interphase (SEI) layers by introducing electrolyte additives and/or solid-state electrolytes and building an artificial interfacial layer have been widely investigated to inhibit the growth of Li dendrites [7–12]. Although these methods could alleviate the growth of Li dendrites to some extent, the infinite relative volume change of Li during the charge–discharge process could inevitably result in large internal stress fluctuation and hence break the SEI layers, leading to unsatisfied cycling performance [13].

To solve this issue, loading Li metal into flexible three-dimensional (3D) conductive scaffolds with high surface area and high mechanical strength has been proposed, which could not only alleviate the volume change of Li but also reduce the current density, leading to the suppressed formation of Li dendrites. Particularly, owing to their light-weight nature and tunable surface chemistry, various carbon materials, e.g., carbon cloth (CC) [14,15], carbon nanofibers [16], carbon nanotubes [17], and graphitic carbon foam [18], have been adopted to host Li metal anode.

* Corresponding authors.
E-mail addresses: xiaguanglin@fudan.edu.cn (G. Xia), zguo@uow.edu.au (Z. Guo), yuxuebin@fudan.edu.cn (X. Yu).

https://doi.org/10.1016/j.jechem.2021.06.001

However, the poor affinity between carbon and Li during initial nucleation process attributed to the large lattice mismatch between hexagonal carbon and the body-centered cubic structured lithium leads to inhomogeneous deposition of Li metal and finally the formation of dendrites. In order to enhance the lithiophilicity of carbon frameworks, two strategies have been mainly adopted. The first one is the modification with nucleation seeds, including metals (e.g., Ag, Au, Zn, Mg) [19–22] or their relative oxides (e.g., ZnO, TiO_2), [23,24] to guide the homogeneous deposition of Li metal. Among them, Zn is capable of enhancing the lithiophilicity of carbon-based substrate attributed to its spontaneous reaction with lithium (*i.e.*, Li + Zn → LiZn) and more importantly, the *in-situ* formed LiZn alloys exhibit strong interaction with lithium, which enables LiZn alloys to subsequently regulate the uniform Li deposition behavior [24]. The alloying reactions or the conversion reactions occurred during Li plating process, however, generally involves large volume change, which renders the interface between electrolyte and electrode structurally unstable [25]. Hence, the cycling performance of Li metal anodes modified solely by carbon frameworks decorated with nucleation seeds is still unsatisfied. Alternatively, heteroatom doping has been introduced to regulate the adsorption capability of Li on carbon scaffolds towards the favorable Li deposition [26,27]. Unfortunately, the regulation of Li adsorption on the region away from the doped sites remains weak. Therefore, the precise nucleation and orientated growth of lithium, especially under deep stripping and plating, is still a big challenge.

In this work, the synergistic effect of heteroatom doping and nucleation seeds in further enhancing the cycling performance of Li metal anodes is proposed via building a novel hierarchical structure, *i.e.*, Zn nanoparticles embedded in N-doped carbon polyhedra uniformly decorated on carbon cloth. First, the freestanding CC frameworks could not only provide a 3D interconnected skeleton with sufficient voids for rapid electron and ion transport but also preserve the integrality of Li metal anodes upon repeated Li stripping/plating process, thus contributing to the improved cycling performance. More importantly, it is experimentally and theoretically demonstrated that the lithiophilic Zn nanoparticles (NPs) uniformly distributed inside the N-doped carbon networks in Zn@NC derived from the carbonization of ZIF-8 plays a synergistic role in enhancing the lithophilic ability of CC frameworks, which could effectively reduce Li deposition overpotential, guide the uniform Li deposition, and eventually eliminate the growth of lithium dendrites. Furthermore, the porous N-doped carbon polyhedras help to not only relieve the volume change of Li but also maintain the structural stability of Zn NPs as the nucleation seeds during plating and striping, leading to a well-preserved cycling stability. As a result, the Li-Zn@NC@CC electrode exhibited stable cycling performance at a current density of 1 mA cm^{-2} for over 1200 h and maintained a high CE of 95.4% after 40 cycles under a deep areal capacity of 12 mA h cm^{-2}, which is much superior than Li metal anodes modified by carbon cloth decorated with Zn NPs or N-doped carbon polyhedra. Moreover, the full cells coupled with a $LiFePO_4$ cathode delivered a large reversible capacity of 110.2 mA h g^{-1} with a capacity retention of 78% after over 200 cycles.

2. Experimental

2.1. Preparation of Zn@NC@CC and NC@CC

The commercial carbon cloth (CC, WOS1002, CeTech) was first cleaned by concentrated hydrochloric acid at 80 °C for 2 h and then washed with distilled water. Subsequently, the treated CC dried at 60 °C was cut into pieces (3 × 5 cm) and immersed in PVP solution (2 mg mL^{-1}) with ultrasonic treatment for 40 min, which was then mixed with 2-methylimidazole (2.62 g, 98%, Adamas-beta) dissolved in methanol (50 mL). Meanwhile, 1.19 g zinc nitrate hexahydrate ($Zn(NO_3)_2{\cdot}6H_2O$, 99%, Aladdin) dissolved in methanol (50 ml) was slowly added to the former solution under stirring for 30 min. After aged at room temperature for 24 h, the ZIF-8@CC was obtained after washing with distilled water and drying. Afterwards, the obtained ZIF-8@CC was heated to 600 °C with a heating rate of 5 °C min^{-1} in Ar/H_2, followed by thermal annealing at this temperature for 4 h to synthesize Zn@NC@CC. The NC@CC composite was prepared by soaking the Zn@NC@CC composite in HCl solution for a whole night to remove Zn NPs.

2.2. The preparation of Zn@CC

Specifically, 0.734 g $(CH_3COO)_2Zn$ and 0.320 g NaOH were dissolved in 60 mL deionized water and a piece of carbon cloth (CC) was immersed in this solution and stirred for 30 min, which was subsequently transferred into a 100 mL Teflon-lined stainless autoclave for reaction at 160 ℃ for 20 h. After the autoclave cooled down to room temperature, the as-obtained product was washed with distilled water and dried in an oven at 80 ℃ for several times, yielding the product of ZnO@CC. Afterwards, the as-synthesized ZnO@CC was heated to 600 °C for 4 h with a heating rate of 5 °C min^{-1} in Ar/H_2 to obtain Zn@CC.

2.3. Material characterizations

The crystalline structure of all samples was identified by X-ray diffraction (XRD; D8 advance, Bruker AXS) with Cu *K*α radiation at a scanning rate of 5° min^{-1}. Scanning electron microscopy (SEM, Shimadzu JEOL 7500FA) was conducted to determine the morphology and particle sizes of the samples. Elemental analyses of the materials were tested by energy-dispersive X-ray spectroscopy (EDS) on SEM. All samples that are easily oxidized in the air were pretreated by sealing on sample stage in the Ar-filled glovebox with scotch tapes before testing. X-ray photoelectron spectroscopy (XPS, Escalab 250Xi Thermo Fisher Scientific) test was performed by using Al *K*α radiation (*E* photon = 1486.6 eV) to characterize the surface composition. The surface areas were calculated by the nitrogen adsorption and desorption isotherms via the Brunauer-Emmett-Teller (BET) method.

2.4. Electrochemical measurements

The Zn@NC@CC, NC@CC, Zn@CC and CC composites were cut into disks with a diameter of 11 mm and then adopted as the working electrode to assemble coin cells in an argon filled glove box for electrochemical testing. The thickness of these disks were controlled to be approximately 250 μm.

For symmetric cell testing, Li was firstly deposited with a capacity of 12 mA h cm^{-2} on Zn@NC@CC, NC@CC, and CC disks, respectively, at a current density of 0.5 mA cm^{-2} to form Li-Zn@NC@CC, Li-NC@CC, and Li-CC electrodes. The thickness of these electrodes was approximately 270 μm. The cycling performance of these symmetric cells was tested at various current densities of 0.5, 1.0, and 3.0 mA cm^{-2}, respectively. Celgard 2400 was used as the separator and the electrolyte was lithium bis(trifluoromethanesulfonyl)imide (LiTFSI, 1 M, 99.95%, Sigma-Aldrich) in a mixture solvent of 1,3-dioxolane (DOL, 99%, Sigma-Aldrich) and dimethoxyethane (DME, 99.5%, Sigma-Aldrich) (1:1, volumetric ratio) with 2 wt% $LiNO_3$. Full cells were assembled using $LiFePO_4$ cathode prepared by mixing $LiFePO_4$ powder (Shenzhen Dynanonic Co., Ltd), Super P (Sigma-Aldrich), and polyvinylidene difluoride (PVDF, Shanxi Lizhiyuan Battery Material Co. Ltd) with a weight ratio of 8:1:1. The low and high mass loading of the LFP cathodes was controlled to

be about 2.5 mg cm^{-2} and 13.5 mg cm^{-2}, respectively. The as-prepared Li-Zn@NC@CC, Li-CC, and bare Li electrodes were used as anodes. (the capacity of Li loading was controlled to be 12 mA h cm^{-2}). The negative/positive electrode capacity ratio was controlled to be approximately 28 (the mass loading of LFP is about 2.5 mg cm^{-2}) and 5.2 (the mass loading of LFP is about 13.5 mg cm^{-2}), respectively. The thickness of bare Li anode adopted in the half cell and symmetric cells was approximately 510 μm and this value was approximately 100 μm in the full cells. All full cells were tested in the voltage window between 2.5 and 4.0 V at various current densities, and electrochemical impedance spectroscopy (EIS) was tested in a frequency range from 100 KHz to 0.01 Hz.

2.5. Computational method

Density functional theory (DFT) calculations were carried out using projector-augmented wave (PAW) method as implemented in Vienna ab initio simulation package (VASP) [28–30]. A generalized gradient approximation (GGA) of Perdew-Burke-Ernzerhof (PBE) functional was employed to describe the exchange–correlation interaction [31]. An energy cutoff of 500 eV and Gamma centered 5 × 5 × 1 k-points mesh were applied to all calculations. The structures were relaxed until the forces and total energy on all atoms were converged to less than 0.05 eV $Å^{-1}$ and 1×10^{-5} eV. The Zn (0001) and Li (001) slab models were the cleaved surface of each metal with the lowest surface energy, and a four-layer 4 × 4 × 1 super cell with 20A vacuum was adopted. To evaluate the interaction between Li and electrode, the binding energy (E_b) was calculated as follows,

$$E_b = E_{Total} - E_{Li} - E_{sub}$$

where E_{sub} and E_{Total} are the total energy of compound before and after Li adsorption, respectively. E_{Li} is the energy of a single Li atom.

3. Results and discussion

The synthetic process of Li-Zn@NC@CC electrode is schematically illustrated in Fig. 1a. First, the CC substrates treated with the acid and polyvinyl pyrrolidone (PVP) dissolved in methanol were mixed with Zn metal ions (Zn^{2+}) and N-containing 2-methylimidazole solution to form ZIF-8 on the surface of CC substrates (denoted as ZIF-8@CC) by a solution deposition route at room temperature. After the solution deposition process, XRD pattern illustrates the characteristic peaks of ZIF-8 (Fig. S1a), indicating the successful formation of ZIF-8 with high purity [32]. More interestingly, induced by the presence of PVP, which serves as the structure-directing agent for the nucleation and growth of ZIF-8, the thus-formed ZIF-8 are uniformly distributed on the CC substrates as evidenced by the SEM images (Fig. 1g), which turns the color of CC substrates from black into white (Fig. 1c). Subsequently, the as-obtained ZIF-8@CC was thermally annealed in an Ar/H_2 atmosphere to reduce the Zn^{2+} into metallic Zn NPs and transform the imidazolate linkers into N-doped carbon frameworks, leading to the formation of Zn NPs embedded in N-doped carbon polyhedra uniformly decorated on carbon cloth (denoted as Zn@NC@CC). After the carbonization process, the color of the CC substrate transforms into black again (Fig. 1d) and the uniform distribution of Zn@NC with an average size of 250 nm is well preserved due to the structural support role of CC substrate (Fig. 1h). The energy dispersive X-ray (EDX) spectrum reveals the presence of C, N, and Zn in the as-synthesized Zn@NC@CC (Fig. 1i), which agrees well with the XPS results. Meanwhile, the corresponding elemental mapping demonstrates the uniform distribution of the elemental Zn, N, and C element is comparable with the map of Zn@NC@CC, indicating the homogeneous distribution of Zn, N, and C in the as-prepared Zn@NC@CC. In order to further characterize the structure of the as-prepared Zn@NC in detail, transmission electron microscopy (TEM) measurement was conducted (Fig. S2), which validates the typical porous structure of Zn@NC. The corresponding elemental mapping results demonstrate that the Zn, N, and C elements are uniformly distributed across the whole Zn@NC polyhedra, which provides additional evidence to the homogeneous distribution of Zn NPs inside of the as-prepared Zn@NC polyhedra. Based on the thermogravimetric analysis (TGA) results under air atmosphere (Fig. S3), the amount of Zn NPs in the as-synthesized Zn@NC@CC was calculated to be approximately 3.9%. No characteristic peaks, however, could be observed in the XRD results in the resulting Zn@NC@CC (Fig. S1b), coinciding well with previous reports [22,33], which could be attributed to the amorphous nature of Zn NPs and/or the ultralow content of Zn NPs in the as-prepared Zn@NC@CC. The formation of Zn could be clearly validated by the high-resolution XPS results, which exhibits typical peaks at 1021.8 and 1044.7 eV that are indexed to metallic Zn (Fig. S4a) [22,33]. In addition, the spectra of C 1 *s* exhibits two major peaks at 285.5 and 287.1 eV (Fig. S4b), which could be indexed to C–C/C = C and C-N, respectively. Three peaks, which could be assigned to pyridinic N at 397.5 eV, pyrrolic N at 399.4 eV, and graphitic N at 402.3 eV, respectively, are observed in the spectrum of N 1 s, demonstrating the abundant of N inside of carbon frameworks (Fig. S4c) [34]. N_2 adsorption/desorption measurements were further used to assess the Brunauer–Emmett–Teller (BET) surface area of Zn@NC@CC. It is interesting to note that compared to the pure CC with a specific surface area of only 19.6 $m^2 g^{-1}$ (Fig. S5b), the BET surface area was increased to 117.9 $m^2 g^{-1}$ for the Zn@NC@CC owing to the vast introduction of porous structure of Zn@NC (Fig. S5a). It could not only provide more spaces for accommodating the volume change of Li deposition, but also reduce the local current density towards uniform Li deposition [16]. Finally, Li metal was electroplated at a current density of 0.5 mA cm^{-2} into Zn@NC@CC hosts to obtain a Li loading capacity of 12 mA h cm^{-2}, denoted as Li-Zn@NC@CC, which presents a uniform metallic appearance (Fig. 1e).

The Li plating performance of Zn@NC@CC was subsequently investigated using coin cells. According to the voltage-capacity profile (Fig. 2b and Fig. S6a), an obvious overpotential of over 11 mV could be observed for Li-CC electrode. After modification of CC with N-doped carbon frameworks to form NC@CC, which was prepared via the etching of Zn NPs from Zn@NC@CC, the overpotential could be decreased to 9.6 mV for Li-NC@CC, indicating the positive role of N-doping in improving the lithiophilic ability of carbon frameworks. In strong contrast, almost no nucleation overpotential could be observed in the Li plating process of Li-Zn@NC@CC anode, which directly demonstrates the synergistic role of lithiophilic Zn NPs and N-doping of Zn@NC@CC in enhancing the lithiophilicity of carbon frameworks. The discharging capacity over 0 V could be mainly attributed to the insertion of Li^+ into C with the formation of Li_xC_6 and the alloying reaction between Li and Zn [35–37]. Upon decreasing the voltage to below 0 V, metallic Li via the reduction of Li ions began to grow on the Zn@NC@CC. When the deposition capacity of Li reaches 8 mA h cm^{-2}, the top surface (the side near the separator) of Zn@NC@CC electrode is covered with a thin lithium layer, while the bottom surface (the side away from the separator) remains black, indicating the uniform plating of the metallic Li on the top layer of Zn@NC@CC at this stage. Upon increasing the deposition capacity of Li to 12 mA h cm^{-2}, the thin lithium layer covered on the top surface becomes denser with the appearance of a few pockets of Li metal appears on the bottom surface of Li-Zn@NC@CC electrode (Fig. S6b). More interestingly, continuous growth of Li was observed on the bottom surface of Zn@NC@CC with the further increase of Li deposition capacity to 16 and 20 mA h cm^{-2} (equaling

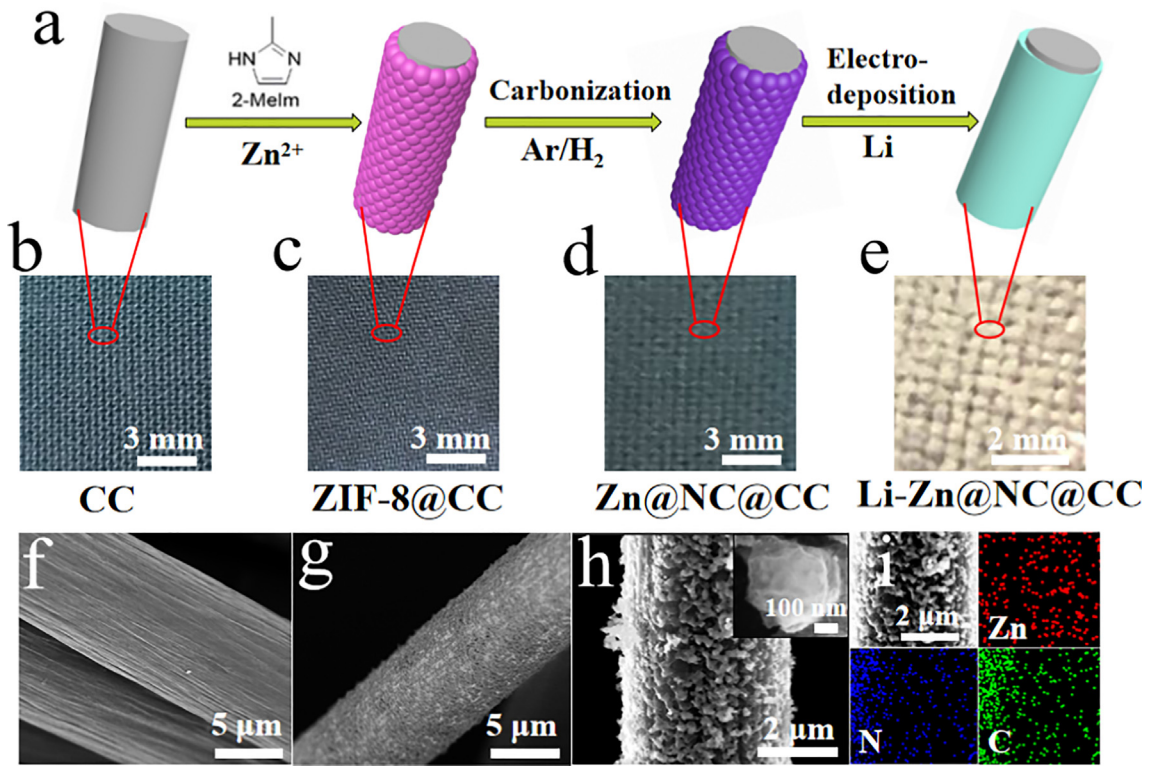

Fig. 1. (a) Schematic synthesis process of Li-Zn@NC@CC electrode. Digital images of the as-prepared CC (b), ZIF-8@CC (c), Zn@NC@CC (d), and Li-Zn@NC@CC (e), respectively. SEM images of CC (f), ZIF-8@CC (g), and Zn@NC@CC (h). (i) SEM image and the corresponding elemental mapping of Zn@NC@CC.

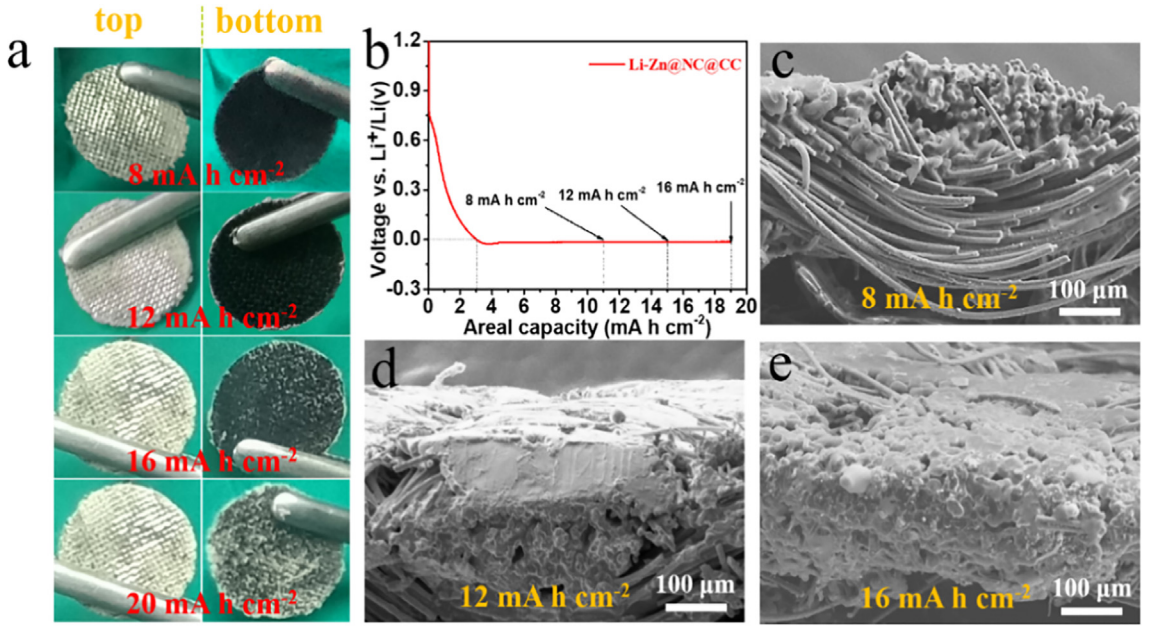

Fig. 2. (a) Digital images of Li-Zn@NC@CC electrode after Li plating with various area capacities. (b) Voltage-capacity profile of Li deposition process of Li-Zn@NC@CC. Cross-sectional SEM images of Li-Zn@NC@CC electrode after Li plating for 8 mA h cm^{-2} (c), 12 mA h cm^{-2} (d), and 16 mA h cm^{-2} (e).

to a specific capacity of 990 mA h g^{-1}) while maintaining the compact and smooth structure of Li on top surface, suggesting that metallic Li could be uniformly deposited on Zn@NC@CC from top to bottom layers along the carbon fibers (Fig. 2a). Cross-sectional SEM images provide further evidence to the uniform Li deposition on the top layer of Zn@NC@CC host at the initial plating process. Upon the increase of Li plating capacity, metallic Li would continue to deposit inside the space between carbon fibers and grow along carbon fibers towards the direction of the bottom layer of Zn@NC@CC host under the guidance of Zn NPs and N-containing carbon network without the observation of any Li dendrites (Fig. 2c-2e). These results confirm that the modification of CC with Zn@NC could effectively alleviate the volume change of Li and prevent the growth of Li dendrite during Li stripping/plating process. In strong contrast,

under a Li plating of only 12 mA h cm^{-2} using the identical condition, the formation of metallic Li could be randomly observed on both the top and the bottom surface of CC electrode in disorder (Fig. S6c). This phenomenon is further verified by SEM images, which validates the uneven distribution of Li inside the gaps between carbon fibers and on the surface of CC substrate for Li-CC electrode with the rough surface (Fig. S10b and S10d), indicating the uncontrollable Li plating behavior due to the lithiophobic nature of carbon. After the etching of Zn NPs from Zn@NC@CC, metallic Li was densely plated on top surface of CC with the observation of few Li metals on the bottom side (Fig. S6c). It directly demonstrates that both the doping of N and the modification of lithiophilic Zn seeds play a synergistic role in improving the uniform Li deposition behavior on CC. It is well known that the electrochemical deposition of Li metal is controlled by the competition between the speed of electron transfer and the Li ion diffusion [38]. At the beginning of Li plating process, the electronic conductivity of the whole Zn@NC@CC is relatively uniform due to the high electronic conduction of CC as the structural support, while Li ions from the counter electrode are initially concentrated on the top surface of Zn@NC@CC electrode. Hence, the plating of Li metal could be initially observed on the top surface of Zn@NC@CC electrode. Upon the proceeding of the deposition, the accumulation of plated Li on the surface of Zn@NC@CC could slow down the electron transfer kinetics in the top surface of the whole electrode due to the relatively low electronic conductivity of Li and more importantly, it would also weaken the binding capability of Zn and N-doped carbon towards Li ions. As a result, the deposition of Li metal would occur along the carbon fibers towards the bottom layer of the Zn@NC@CC hosts upon the continuous increase of the Li deposition capacity as evidenced by SEM images (Fig. 2c-2e).

To understand the mechanism behind the synergistic effect of Zn NPs and N-doping in guiding uniform Li deposition, the binding energies between Li and Zn NPs and N-rich carbon were evaluated by calculating their binding energies based on density functional theory (DFT) calculations. The binding energy between Li atom and Li (001) surface is first calculated to be −1.44 eV as a critical value, and all the calculated binding energies, as well as the optimized adsorption configurations of a Li atom on various substrates, are summarized in Fig. 3a. Among them, the defect-free (-1.34 eV) and graphitic-N-doped carbon (-0.93 eV) exhibit a relatively larger binding energy than that of Li (001) plane, which demonstrates their lithiopholic nature and thus favors the formation of Li dendrites on their surfaces [39]. In contrast, the binding energy between Li atom and Zn (0001) plane could reach a low value of −2.34 eV and this value is further reduced to be as low as −4.31 eV and −4.95 eV for pyridinic-N and pyrrolic-N doped carbon, respectively, which have been verified to be main components of Zn@NC@CC. These results directly confirm that Zn NPs and N-rich carbon of Zn@NC could serve as effective lithiophilic sites for the uniform nucleation and growth of plated Li. Subsequently, the models composed of Zn distributed on N-doped carbon were built to evaluate their synergistic effect in enhancing the lithiophilic capability of carbons (Fig. 3h-3k). It is interesting to note that, under a stable structural configuration, the binding energies of Zn distributed on N-doped carbons exhibit a much lower binding energy than that of both Zn and N-doped carbon under a stable structural configuration. It verified the synergistic effect of Zn and N-doping in Zn@NC in enhancing lithiophilicity of CC, which could hence induce the uniform deposition of Li on the surface of CC. Therefore, combined with the porous structure of Zn@NC@CC, which plays an important role in accommodating the volume change of Li plating and reducing the local current density, the as-prepared Zn@NC@CC could effectively suppress the formation of Li dendrites.

The electrochemical performance of Li-Zn@NC@CC was subsequently evaluated in symmetric cells with a fixed capacity of

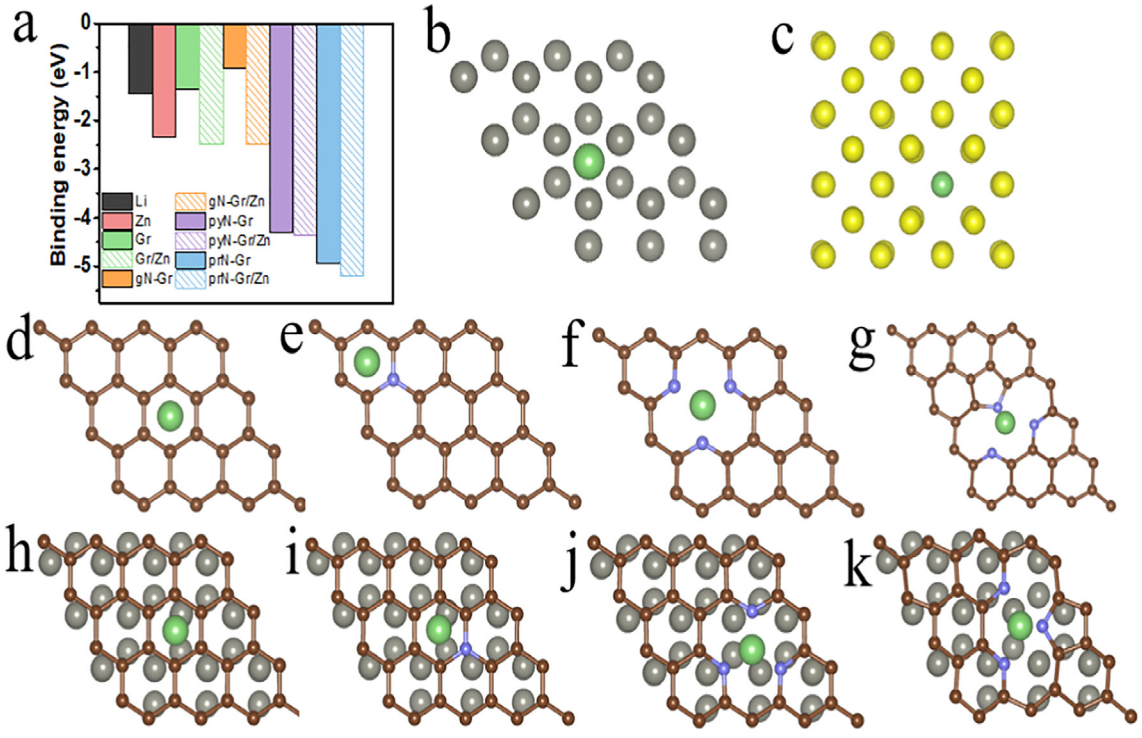

Fig. 3. (a) The summary of calculated binding energies between Li and various substrates. The optimized adsorption configurations of Li on (b) Zn (0001) surface, (c) Li (001) surface, and (d) defect-free (Gr), (e) graphitic-N (gN-Gr), (f) pyridinic-N (pyN-Gr), and (g) pyrrolic-N (prN-Gr) doped carbon sheet. The optimized adsorption configurations of Li on Zn under the support of carbon sheets, i.e., (h) Gr/Zn, (i) gN-Gr/Zn, (j) pyN-Gr/Zn, and (k) prN-Gr/Zn composites. The grey, yellow, green, blue, and brown balls represent Zn, Li, adsorbed Li, N, and C atoms, respectively.

1 mA h cm^{-2}, with Li-NC@CC, Li-CC, and bare Li electrodes included for comparison. As expected, a continuous increase of overpotential to 38 mV could be observed for bare Li after only 400 h due to the severe reaction between electrolyte and Li metal upon cycling process. Owing to the presence of CC as the structural support, the increase of overpotential could be alleviated for Li-CC with an overpotential of 20 mV after 550 h. Interestingly, in the term of Li-NC@CC, a stable cycling life of over 800 h was achieved, which further demonstrates that N-doping could enhance the cycling stability of Li plating/stripping process due to the improved adsorption capability of nanostructured carbon with Li. By comparison, induced by the synergistic role of Zn NPs and N-doping, Li-Zn@NC@CC anode displays an ultralow overpotential of ~ 9 mV for over 1300 h (Fig. 4a). When the current density increases to 1 mA cm^{-2}, Li-Zn@NC@CC anode can also maintain a small overpotential of 14 mV for 1200 h (Fig. 4b), much superior than that of Li-NC@CC, Li-CC, and bare Li electrodes. Upon increasing the current density to 3 mA cm^{-2}, the voltage hysteresis of Li-CC reaches ~ 400 mV after only 176 h. It is interesting to note that, upon decorating CC with Zn NPs (denoted as Zn@CC), the cycling life of the as-prepared Li-Zn@CC electrode could be extended to 270 h with a low voltage hysteresis of 39 mV (Fig. S8) and a stable cycling performance of over 220 h with a voltage hysteresis of 36 mV could also be observed for the Li-NC@CC anode. It directly demonstrates the positive role of both Zn and N-doped carbon in improving the stability of Li metal anodes. More impressively, Li-Zn@NC@CC remains stable for nearly 400 h with smooth voltage plateaus and a low voltage hysteresis of ~ 38 mV (Fig. 4c). These results provide direct evidence to the synergistic effect of Zn and N-doped carbon in promoting uniform Li deposition into carbon cloth.

In order to further understand the mechanism of the enhanced electrochemical performance induced by Zn@NC@CC, SEM was used to characterize the morphology change of electrodes upon cycling. Compared to the pristine Li foils with smooth and flat surface (Fig. S10a and S10c), a large amount of porous structures com-

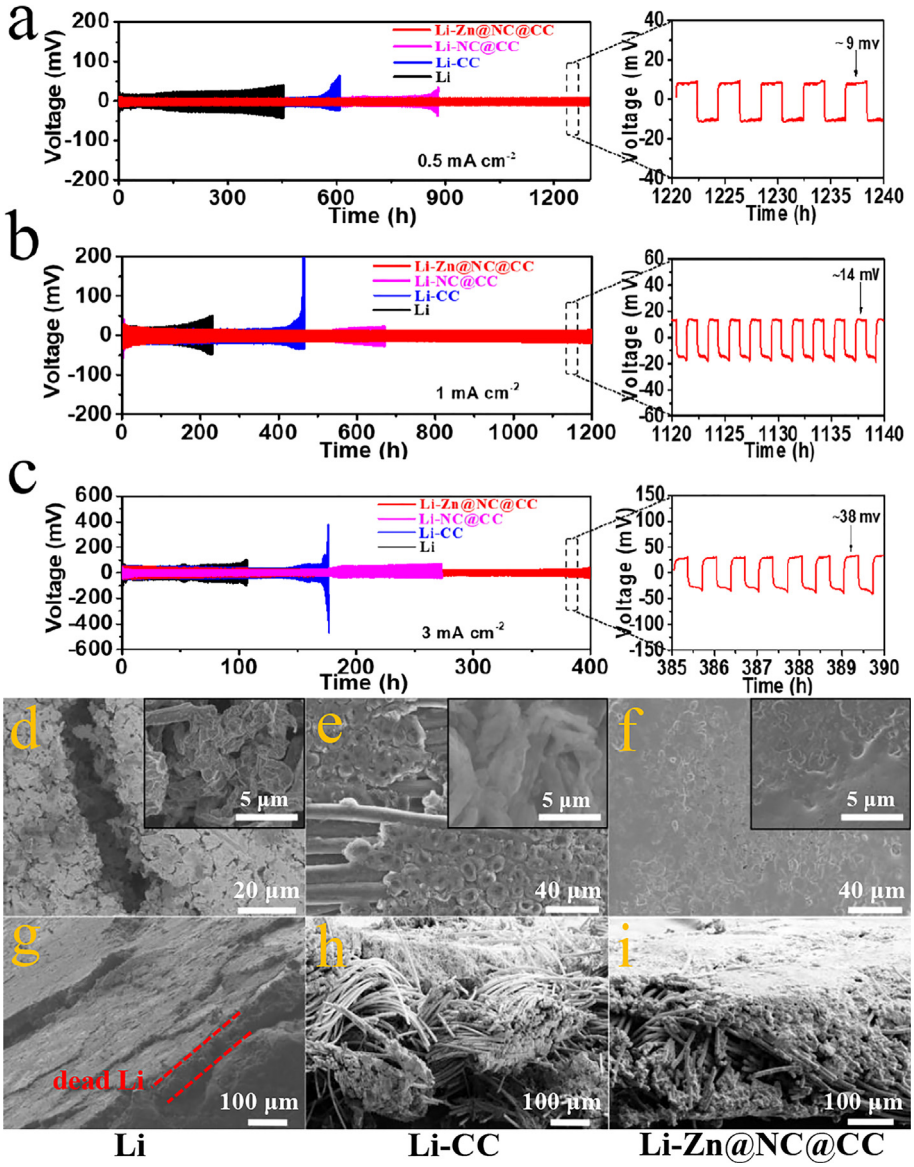

Fig. 4. Voltage profiles of Li plating/stripping in Li-Zn@NC@CC, Li-NC@CC, Li-CC, and bare Li symmetric cells with a fixed capacity of 1 mA h cm^{-2} at the current density of 0.5 (a), 1 (b), and 3 mA cm^{-2} (c), respectively. Enlarged figures on the right are detailed voltage profiles of selected cycles. Top-view and cross-sectional SEM images of (d, g) bare Li, (e, h) Li-CC, and (f, i) Li-Zn@NC@CC electrodes after 100 cycles in symmetrical cells at 1 mA cm^{-2} for 1 mA h cm^{-2}.

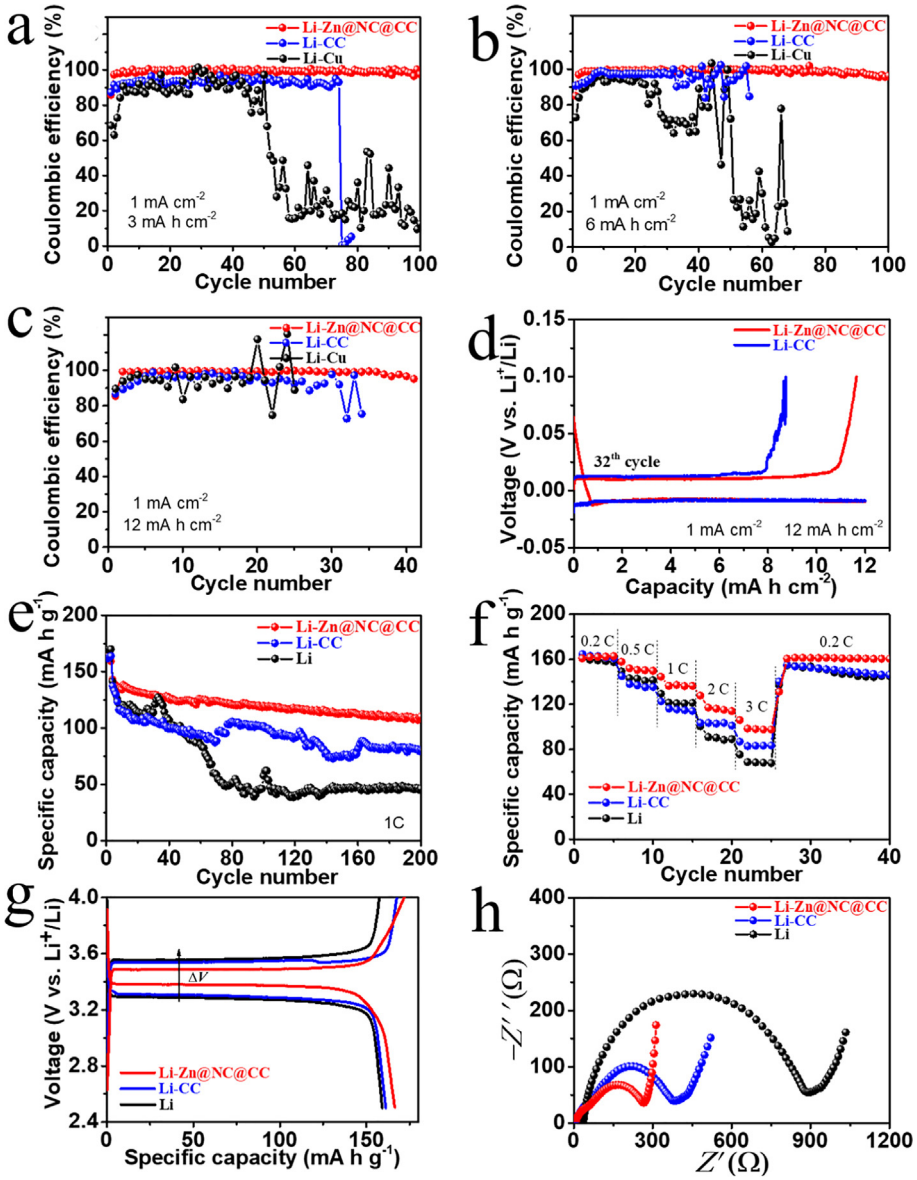

Fig. 5. Coulombic efficiencies of Li-Zn@NC@CC, Li-CC, and Li-Cu electrodes at a stripping/plating current density of 1 mA cm^{-2} for 3 mA h cm^{-2} (a), 6 mA h cm^{-2} (b), and 12 mA h cm^{-2} (c), respectively. (d) The corresponding voltage profiles of Li plating/stripping at the 32th cycle of Li-Zn@NC@CC and Li-CC electrodes. (e) Cycling performance of Li-Zn@NC@CC//LFP, Li-CC//LFP, and Li//LFP full cells at 1C (1C = 170 mA g^{-1}). (f) Rate capability of Li-Zn@NC@CC//LFP, Li-CC//LFP, and Li//LFP full cells. (g) Voltage profiles for Li-Zn@NC@CC//LFP, Li-CC//LFP, and Li//LFP full cells at the current density of 1C. (h) The electrochemical impedance spectra of Li-Zn@NC@CC//LFP, Li-CC//LFP, and Li//LFP full cells after 200 cycles.

posed of Li dendrites and cracks (Fig. 4d and 4 g) are present on its surface accompanied with the formation of "dead Li" after 100 cycles. Although CC in Li-CC electrode could effectively alleviate the volume change of Li and reduce the current density, the growth of Li dendrites could still be randomly observed after cycling due to the lithiophobic nature of pure CC substrate (Fig. 4e and 4 h). By comparison, after identical Li stripping/plating processes, the Li-Zn@NC@CC electrode presents constant morphology without the observation of any Li dendrites and pulverization (Fig. 4f and 4i), which directly confirms that the Li-Zn@NC@CC electrode can effectively suppress the formation of Li dendrites and "dead" Li over long-term cycling. In addition to the surface investigation of the Li-Zn@NC@CC electrode, SEM image validates the uniform plating of Li along the surface of Zn@NC@CC in the interior space of Li-Zn@NC@CC electrode after cycling without the observation of any Li dendrites or dead Li (Fig. S12). Moreover, the corresponding elemental mapping results demonstrate that the uniform distribution of N and Zn elements inside of Li-Zn@NC@CC electrode could be well preserved upon cycling, which contributes to enhancing the cycling stability of the uniform Li plating and stripping process.

The reversible stability of Zn@NC@CC host was subsequently evaluated in half cells at 1.0 mA cm^{-2} using Cu, CC, and Zn@NC@CC as the working electrode and Li foil as the reference electrode. Due to the significant side reaction between deposited Li and the electrolyte, the coulombic efficiencies on bare Cu electrodes significantly decreases upon cycling charge–discharge process with a plating capacity of 3 mA h cm^{-2} after only 40 cycles and the cycling life is further reduced to 20 cycles upon increasing the plating capacity of 6 mA h cm^{-2}. The coulombic efficiencies could be slightly enhanced when using CC as the structural support, but still unsatisfactory upon long-term cycling process. In strong contrast, at a relatively low Li plating capacity of 3 mA h cm^{-2} and 6 mA h cm^{-2}, the CE of Zn@NC@CC half cells is maintained at 98.1% and 96.3% over 100 cycles, respectively (Fig. 5a and 5b).

More impressively, as the Li plating capacity increases to 12 mA h cm^{-2}, the Zn@NC@CC half-cells still exhibit a superior electrochemical reversibility with the coulombic efficiencies over 95% after 40 cycles (Fig. 5c and 5d), which provides additional evidence to the high reversibility of Li stripping/plating process on Zn@NC@CC.

To demonstrate the capability of Li-Zn@NC@CC electrode in practical application, full cells were assembled with commercialized $LiFePO_4$ (LFP) as the cathode. The Li-Zn@NC@CC//LFP full cells exhibit stable cycling performance with a reversible capacity of 110.2 mA h g^{-1} at 1C (1C = 170 mA g^{-1}) after 200 cycles, corresponding to a capacity retention of 78%, whereas the reversible capacity rapidly decreased to 80.7 mA h g^{-1} and 46.7 mA h g^{-1} for Li-CC//LFP full cells and Li//LFP half cells, respectively (Fig. 5e). The coulombic efficiencies of Li-Zn@NC@CC//LFP full cells are as high as about 99.5% after 200 cycles at 1C, corresponding well with its excellent cycling stability (Fig. S14). In addition, Li-Zn@NC@CC//LFP full cells exhibit a stable charge/discharge plateau with a voltage hysteresis ($\triangle V$) of only 108 mV at 1C, much lower than that of Li-CC//LFP full cells and Li//LFP half cells (Fig. 5g), which agrees well with their results in Li plating/stripping process. Besides, the rate performances demonstrate that the Li-Zn@NC@CC//LFP full cells exhibits highest reversible capacities at all current densities. Specifically, the Li//LFP half cell presents a noticeable capacity decay from 157.3 mA h g^{-1} at 0.2C to 67.6 mA h g^{-1} at 3C, and the reversible capacity also decreases to 83.2 mA h g^{-1} at 3C for Li-CC//LFP full cell. By comparison, Li-Zn@NC@CC//LFP full cell could still maintain a reversible capacity of 97.5 mA h g^{-1} even at a rate of 3C (Fig. 5f). The charge-transfer resistance (*R*ct), which is a key indicator for evaluating the kinetics of the electrode, was calculated based on the fitting results of electrochemical impedance spectroscopy (EIS) results according to the equivalent circuit model (Table S1). It is revealed that the *R*ct at the interface between electrode and electrolyte of Li-Zn@NC@CC//LFP full cell is only 210.7 Ω, whereas this value is increased to be 842.4 Ω and 377 Ω for Li//LFP and Li-CC//LFP full cell, respectively (Fig. 5h), which suggests that the excellent rate capability of Li-Zn@NC@CC//LFP full cell could be attributed the low interfacial resistance and fast kinetics. The areal mass loading of the LFP cathode was further increased to 13.5 mg cm^{-2} for investigating the potential application of Li-Zn@NC@CC under practical conditions. Impressively, the Li-Zn@NC@CC//LFP full cell still remains a high reversible capacity of 109.3 mA h g^{-1} over 160 cycles at 1C, which is comparable to that of full cells with a low mass loading of the LFP cathode (112.1 mA h g^{-1}). In addition, rate performance validates that the Li-Zn@NC@CC//LFP full cell could deliver a high reversible capacity of 82.7 mA h g^{-1} at 2C, and this value could return to 121.1 mA h g^{-1} when the current density was reduced back to 0.5C (Fig. S15), suggesting the stable reversibility of Li stripping and plating process. The SEM images also validate that the Li-Zn@NC@CC electrode exhibits more uniform and smooth surface than that of both pristine Li and Li-CC electrode after cycling (Fig. S16), which provides further evidence to the excellent stability of Li-Zn@NC@CC electrode upon charge–discharge process, leading to superior cycling stability.

4. Conclusion

In this work, a novel Zn@NC@CC host has been synthesized for designing dendrite-free Li metal anode. Owing to the synergistic role of Zn NPs and N-doping inside of porous carbon polyhedra in improving the adsorption capacity with Li, uniform Li deposition along the carbon fibers of carbon cloth could be realized with the complete suppression of Li dendrites. In addition, the uniform distribution of porous N-doped carbon polyhedra on carbon cloth with high mechanical strength could effectively accommodate the volume change of the electrode upon repeated Li stripping/-plating process, leading to the well-preserved structural integrity of the whole electrode and hence excellent long-term cycling stability. Consequently, the Li-Zn@NC@CC electrode exhibits a stable cycling performance for over 1200 h at 1 mA cm^{-2} without voltage fluctuation. When coupled with $LiFePO_4$ cathode, a reversible capacity of 110.2 mA h g^{-1} with a capacity retention of over 78% are achieved in Li-Zn@NC@CC//LFP full cells at 1C after 200 cycles. This strategy opens up new strategies in the reasonable design of stable Li metal anodes for high-energy–density Li metal batteries.

Declaration of Competing Interest

The authors declare that they have no known competing financial interests or personal relationships that could have appeared to influence the work reported in this paper.

Acknowledgments

This work was partially supported by the National Science Fund for Distinguished Young Scholars (51625102), the National Natural Science Foundation of China (51971065, 51901045), the Innovation Program of Shanghai Municipal Education Commission (2019-01-07-00-07-E00028), the Programs for Professor of Special Appointment (Eastern Scholar) at Shanghai Institutions of Higher Learning, the National Natural Science Foundation of China (NSFC − U1903217), and the National Natural Science Foundation of China (No. 21978073).

Appendix A. Supplementary data

Supplementary data to this article can be found online at https://doi.org/10.1016/j.jechem.2021.06.001.

References

[1] J.B. Goodenough, Y. Kim, Chem. Mater. 22 (2010) 587–603.
[2] W. Xu, J. Wang, F. Ding, X. Chen, E. Nasybulin, Y. Zhang, J.G. Zhang, Energy Environ. Sci. 7 (2014) 513–537.
[3] D.C. Lin, Y.Y. Liu, Y. Cui, Nat. Nanotechnol. 12 (2017) 194–206.
[4] Y.Y. Wang, Z.X. Zhao, W. Zeng, X.B. Liu, L. Wang, J. Zhu, B.G. Lu, J. Energy Chem. 58 (2021) 292–299.
[5] J.F. Qian, W.A. Henderson, W. Xu, P. Bhattacharya, M. Engelhard, O. Bordin, J.G. Zhang, Nat. Commun. 6 (2015) 6362–6370.
[6] J. Liu, Z.N. Bao, Y. Cui, E.J. Dufek, J.B. Goodenough, P. Khalifah, Q.Y. Li, B.Y. Liaw, P. Liu, A. Manthiram, Y.S. Meng, V.R. Subramanian, M.F. Toney, V.V. Viswanathan, M.S. Whittingham, J. Xiao, W. Xu, J.H. Yang, X.Q. Yang, J.G. Zhang, Nature Energy 4 (2019) 180–186.
[7] X.B. Cheng, R. Zhang, C.Z. Zhao, F. Wei, J.G. Zhang, Q. Zhang, Adv. Sci. 3 (2016) 1500213–1500232.
[8] W.Y. Li, H.B. Yao, K. Yan, G.Y. Zheng, Z. Liang, Y.M. Chiang, Y. Cui, Nat. Commun. 6 (2015) 7436–7443.
[9] C.Z. Zhao, X.B. Cheng, R. Zhang, H.J. Peng, J.Q. Huang, R. Ran, Z.H. Huang, F. Wei, Q. Zhang, Energy Storage Mater. 3 (2016) 77–84.
[10] N.W. Li, Y.X. Yin, C.P. Yang, Y.G. Guo, Adv. Mater. 28 (2016) 1853–1858.
[11] B. Zhu, Y. Jin, X. Hu, Q. Zheng, S. Zhang, Q. Wang, J. Zhu, Adv. Mater. 29 (2017) 1603755–1603760.
[12] G. Zheng, S.W. Lee, Z. Liang, H.W. Lee, K. Yan, H. Yao, H. Wang, W. Li, S. Chu, Y. Cui, Nat. Nanotechnol. 9 (2014) 618–623.
[13] F. Liu, Q.F. Xiao, H.B. Wu, L. Shen, D. Xu, M. Cai, Y.F. Lu, Adv. Energy Mater. 8 (2018) 1701744–1701750.
[14] Q. Wang, C.K. Yang, J.J. Yang, K. Wu, L.Y. Qi, H. Tang, Z.Y. Zhang, W. Liu, H.H. Zhou, Energy Storage Mater. 15 (2018) 249–256.
[15] K. Li, Z.Y. Hu, J.Z. Ma, S. Chen, D.X. Mu, J.T. Zhang, Adv. Mater. 31 (2019) 1902399–1902407.
[16] K. Lin, X.Y. Qin, M. Liu, X.F. Xu, G.M. Liang, J.X. Wu, F.Y. Kang, G.H. Chen, B.H. Li, Adv. Funct. Mater. 29 (2019) 1903229–1903240.
[17] Z. Liang, D.C. Lin, J. Zhao, Z.D. Lu, Y.Y. Liu, C. Liu, Y.Y. Lu, H.T. Wang, K. Yan, X.Y. Tao, Y. Cui, Proc. Natl. Acad. Sci. USA 113 (2016) 2862–2867.
[18] L. Liu, Y.X. Yin, J.Y. Li, S.H. Wang, Y.G. Guo, L.J. Wan, Adv. Mater. 30 (2018) 1706216–1706223.
[19] K. Yan, Z.D. Lu, H.W. Lee, F. Xiong, P.C. Hsu, Y.Z. Li, J. Zhao, S. Chu, Y. Cui, Nat. Energy 1 (2016) 16010–16017.

[20] S.H. Choi, S.J. Lee, D.J. Yoo, J.H. Park, J.H. Park, Y.N. Ko, J. Park, Y.E. Sung, S.Y. Chung, H. Kim, J.W. Choi, Adv. Energy Mater. 9 (2019) 1902278–1902287.
[21] Q.S. Xu, J.J. Lin, C.C. Ye, X.J. Jin, D.Q. Ye, Y.Y. Lu, G.M. Zhou, Y.C. Qiu, W.S. Li, Adv. Energy Mater. 10 (2019) 1903292–1903300.
[22] M.Q. Zhu, B. Li, S.M. Li, Z.G. Du, Y.J. Gong, S.B. Yang, Adv. Energy Mater. 8 (2018) 1703505–1703511.
[23] J.H. Kim, H.K. Kang, S.G. Woo, G. Jeong, M.S. Park, K.J. Kim, J.S. Yu, T. Yim, Y.N. Jo, H. Kim, K. Zhu, Y.J. Kim, J. Electroanal. Chem. 726 (2014) 51–54.
[24] X.S. Wang, Z.H. Pan, Y. Wu, X.Y. Ding, X.J. Hong, G.G. Xu, M.N. Liu, Y.G. Zhang, W.S. Li, Nano Res. 12 (2019) 525–529.
[25] G. Wang, T. Liu, X.X. Fu, Z.P. Wu, M.L. Liu, X.H. Xiong, Chem. Eng. J. 414 (2021) 128698–128704.
[26] K. Yan, H.W. Lee, T. Gao, G.Y. Zheng, H.B. Yao, H.T. Wang, Z.D. Lu, Y. Zhou, Z. Liang, Z.F. Liu, S. Chu, Y. Cui, Nano Lett. 14 (2014) 6016–6022.
[27] Z.Y. Lu, Q.H. Liang, B. Wang, Y. Tao, Y.F. Zhao, W. Lv, D.H. Liu, C. Zhang, Z. Weng, J.C. Liang, H. Li, Q.H. Yang, Adv. Energy Mater. 9 (2019) 1803186–1803193.
[28] G. Kresse, J. Non. Cryst. Solids 192 (1995) 222–229.
[29] G. Kresse, J. Furthmüller, Phys. Rev. B Condens. Matter. 54 (1996) 11169–11186.
[30] P.E. Blöchl, Phys. Rev. B Condens. Matter. 50 (1994) 17953–17979.
[31] J.P. Perdew, K. Burke, M. Ernzerhof, Phys. Rev. Lett. 77 (1996) 3865–3868.
[32] L.Y. Wang, X.Y. Zhu, Y.P. Guan, J.L. Zhang, F. Ai, W.F. Zhang, Y. Xiang, S. Vijayan, G.D. Li, Y.Q. Huang, G.P. Cao, Y.S. Yang, H. Zhang, Energy Storage Mater. 11 (2018) 191–196.
[33] Z. Wang, J.H. Huang, Z.W. Guo, X.L. Dong, Y. Liu, Y.G. Wang, Y.Y. Xia, Joule 3 (2019) 1289–1300.
[34] T. Zhou, J.D. Shen, Z.S. Wang, J. Liu, R.Z. Hu, L.Z. Ouyang, Y.Z. Feng, H. Liu, Y. Yu, M. Zhu, Adv. Funct. Mater. 30 (2020) 1909159–1909168.
[35] T.S. Wang, X.B. Liu, X.D. Zhao, P.G. He, L.Z. Fan, Adv. Funct. Mater. 30 (2020) 2000786–2000795.
[36] X. Chen, X.R. Chen, T.Z. Hou, B.Q. Li, X.B. Cheng, R. Zhang, Q. Zhang, Sci. Adv. 5 (2019) 7728–7736.
[37] W. Liu, P.C. Liu, D. Mitlin, Chem. Soc. Rev. 49 (2020) 7284–7300.
[38] L.L. Lu, J. Ge, J.N. Yang, S.M. Chen, H.B. Yao, F. Zhou, S.H. Yu, Nano Lett. 16 (2016) 4431–4437.
[39] F. Liu, R. Xu, Z. Hu, S. Ye, S. Zeng, Y. Yao, S. Li, Y. Yu, Small 15 (2019) 1803734–1803744.